DRAFT VERSION APRIL 13, 2017
Preprint typeset using LaTeX style AASTeX6 v. 1.0

arXiv:1704.03481v1 [astro-ph.GA] 11 Apr 2017

THE EDGE–CALIFA SURVEY: VARIATIONS IN THE MOLECULAR GAS DEPLETION TIME IN LOCAL GALAXIES

DYAS UTOMO[1], ALBERTO D. BOLATTO[2], TONY WONG[3], EVE C. OSTRIKER[4], LEO BLITZ[1], SEBASTIAN F. SANCHEZ[5], DARIO COLOMBO[6], ADAM K. LEROY[7], YIXIAN CAO[3], HELMUT DANNERBAUER[8], RUBEN GARCIA-BENITO[9], BERND HUSEMANN[10], VESELINA KALINOVA[6], REBECCA C. LEVY[2], DAMIAN MAST[11], ERIK ROSOLOWSKY[12], AND STUART N. VOGEL[2]

[1]Department of Astronomy, University of California, Berkeley, CA 94704, USA (email: dyas@berkeley.edu)
[2]Department of Astronomy, University of Maryland, College Park, MD 20642, USA
[3]Department of Astronomy, University of Illinois, Urbana, IL 61801, USA
[4]Department of Astrophysical Sciences, Princeton University, Princeton, NJ 08544, USA
[5]Instituto de Astronomía, Universidad Nacional Autónoma de México, A.P. 70-264, 04510 México, D.F., Mexico
[6]Max Planck Institute for Radio Astronomy, Auf dem Hügel 69, D-53121 Bonn, Germany
[7]Department of Astronomy, The Ohio State University, Columbus, OH 43210, USA
[8]Instituto de Astrofísica de Canarias, E-38205 La Laguna, Tenerife, Spain
[9]Instituto de Astrofísica de Andalucía, CSIC, E-18008 Granada, Spain
[10]European Southern Observatory, D-85748 Garching bei München, Germany
[11]Observatorio Astronómico de Córdoba, 5000 Córdoba, Córdoba, Argentina
[12]Department of Physics, University of Alberta, Edmonton, T6G 2E1, Canada

ABSTRACT

We present results from the EDGE survey, a spatially resolved CO(1–0) follow-up to CALIFA, an optical Integral Field Unit (IFU) survey of local galaxies. By combining the data products of EDGE and CALIFA, we study the variation of molecular gas depletion time ($\tau_{\rm dep}$) on kiloparsec scales in 52 galaxies. We divide each galaxy into two parts: the center, defined as the region within $0.1\ R_{25}$, and the disk, defined as the region between 0.1 and $0.7\ R_{25}$. We find that 13 galaxies show a shorter $\tau_{\rm dep}$ ($\sim$ 1 Gyr) in the center relative to the disk ($\tau_{\rm dep} \sim 2.4$ Gyrs), which means the central region in those galaxies is more efficient at forming stars per unit molecular gas mass. This finding implies that the centers with shorter $\tau_{\rm dep}$ resemble the intermediate regime between galactic disks and starburst galaxies. Furthermore, the central drop in $\tau_{\rm dep}$ is correlated with a central increase in the stellar surface density, suggesting that a shorter $\tau_{\rm dep}$ is associated with molecular gas compression by the stellar gravitational potential. We argue that varying the CO-to-H_2 conversion factor only exaggerates the central drop of $\tau_{\rm dep}$.

Keywords: galaxies: star formation — galaxies: structure — ISM: molecules — ISM: abundances.

1. INTRODUCTION

Galactic stellar masses grow through a combination of mergers and the formation of stars from their gas reservoir over cosmic time. Therefore, the star formation rate (SFR) is an important element in driving galaxy evolution (e.g., Kennicutt 1998a; McKee & Ostriker 2007; Kennicutt & Evans 2012). In general, star formation involves two processes: (1) the conversion of diffuse, atomic gas into molecular gas in well-shielded regions of high density, and (2) the dynamical collapse of self-gravitating regions within the molecular component to form stars. In galactic regions with low mean gas volume and low surface density, local gas compression by spiral arms or self-gravity may be needed for molecules to form, whereas in galactic regions of high mean gas volume and surface density, most of the gas may be molecular (e.g., in M51; Schinnerer et al. 2013). In this paper, we focus on the second part of the star formation processes, specifically, we study how the relation between molecular gas and SFR changes between the galactic centers and the disks.

In a simple-minded picture, stars form from the gas that contracts under its self-gravity. Naively, one would expect that the relevant time-scale of this process is the free-fall time ($\tau_{\rm ff}$) of the total gas (atomic and molecular), which is inversely proportional to the square-root of gas volume density ($\rho_{\rm gas}^{-0.5}$). The implication of this simple scenario is that SFR relates to the amount of gas as $\rho_{\rm SFR} \propto \rho_{\rm gas}/\tau_{\rm ff} \propto \rho_{\rm gas}^{1.5}$.[1] In general, the relation between SFR and total gas density is called the Kennicutt-Schmidt (KS) relation, after the seminal papers by Schmidt (1959) and Kennicutt (1998b).[2]

[1] The other time scales that are often used in literature are the orbital time Ω^{-1} (e.g., Elmegreen 1997; Silk 1997), where Ω is the angular speed of the disk, and the vertical time H/σ (Ostriker et al. 2010; Ostriker & Shetty 2011), where H and σ are the thickness and velocity dispersion of the gas.

[2] Actually, Schmidt (1959) proposed $\rho_{\rm SFR} \propto \rho_{\rm gas}^2$ and Kennicutt (1998b) found $\Sigma_{\rm SFR} \propto \Sigma_{\rm gas}^{1.4}$, where Σ is the surface density. Since Σ is the integration of ρ along the projected disk thickness, the translation from $\rho_{\rm SFR}$ to $\Sigma_{\rm SFR}$ depends on the scale height of the ISM.

Observations in the local universe show that stars form in molecular clouds, so we expect that SFR correlates better with the amount of molecular gas, rather than the total amount of atomic plus molecular gas (e.g., Wong & Blitz 2002; Bigiel et al. 2008). Even though the molecular phase may itself not be necessary to form stars (Glover & Clark 2012), molecular gas that forms under the high-density conditions are also favorable to gravitational collapse, thus giving rise to a strong KS relation (Krumholz et al. 2011). For simplicity, in this paper we refer to the relationship between SFR and molecular gas surface densities as the KS relation.

Resolved studies of nearby galaxies found that the correlation between SFR and molecular gas surface densities is approximately linear in galaxy disks, with $\Sigma_{\rm SFR} \propto \Sigma_{\rm mol}$ on kiloparsec (kpc) scales for surface densities $\Sigma_{\rm H2} \gtrsim 3\ M_\odot\ {\rm pc}^{-2}$ over a wide range of local environments (e.g., Bigiel et al. 2008; Leroy et al. 2008). Furthermore, in nearby galaxies, the near-linear molecular KS relation extends to the low metallicity regime ($Z/Z_\odot \approx 0.2$; Bolatto et al. 2011; Jameson et al. 2016) and to the outer part of galaxies, where the gas surface density is low and atomic dominated (Schruba et al. 2011). A possible reason for this widespread relationship is that the properties of molecular clouds are similar from one galaxy and region to another (Bolatto et al. 2008), so that GMCs convert the molecular gas into stars at the same rate (cf. Hughes et al. 2010, 2013; Colombo et al. 2014).

For most of the gas in normal galaxies, the linearity of KS relation implies the molecular gas depletion time, defined as $\tau_{\rm dep} \equiv \Sigma_{\rm mol}/\Sigma_{\rm SFR}$, is approximately constant, with a typical value of ~ 2.2 Gyrs in nearby galaxies (e.g., Bigiel et al. 2008; Leroy et al. 2008; Rahman et al. 2012; Leroy et al. 2013). Loosely, we interpret $\tau_{\rm dep}$ as the time scale to convert all molecular gas reservoir in a galaxy (or a given region within a galaxy) into stars at the current SFR. The fact that $\tau_{\rm dep}$ is less than the Hubble time implies that galaxies need to replenish their gas reservoir through accretion from the intergalactic medium or from their satellite galaxies (e.g., Genzel et al. 2010; Bauermeister et al. 2010; Lilly et al. 2013). However, the direct observational signature of this accretion is still challenging.

Despite the current consensus of the linearity of KS relation in many situations, there are, at least, three regimes where this linearity break down: (1) in the ULIRGs and starburst galaxies, i.e. galaxies above the star forming main-sequence (e.g., Daddi et al. 2010; Genzel et al. 2010, 2015), (2) at resolution finer than $\sim$ 500 pc (e.g., Schruba et al. 2010; Kruijssen & Longmore 2014), and (3) in the galactic centers (e.g., Jogee et al. 2005; Leroy et al. 2013). The steeper-than-linear molecular KS relation in regions of very high molecular surface density has been interpreted as a result of higher molecular gas pressure (Ostriker & Shetty 2011) and density (Krumholz et al. 2012). Higher pressure requires a higher star formation rate per unit molecular mass to offset enhanced turbulent dissipation and cooling, and higher density is associated with shorter dynamical times, which control gravitational contraction.

In this paper, we study the variations of $\tau_{\rm dep}$ between galactic centers and disks by combining the CO data from the EDGE survey (Bolatto et al. 2017) and the optical IFU data from the CALIFA survey (Sánchez et al. 2012), with a goal to quantify and understand the cause of those variations and its implications in galaxy evolution. This paper is organized as follows. Overviews of the EDGE and CALIFA data products and the sample selection are described in §2 and §3, respectively. Then, in §4 we compare $\tau_{\rm dep}$ in the centers relative to those in the disk. Specifically, we investigate whether the difference of $\tau_{\rm dep}$ between the centers and the disks is driven by the star formation rate or molecular gas surface density. In §5, we discuss the effect of the CO-to-H_2 conversion factor, and the connection between $\tau_{\rm dep}$, oxygen abundance, and the size of stellar and molecular gas disk. Lastly, we summarize our findings in §6.

2. DATA DESCRIPTIONS

2.1. *The EDGE Survey*

The EDGE survey targets 126 galaxies in the CO(1–0) and ^{13}CO(1–0) lines using the CARMA observatory (Bock et al. 2006) in the D and E arrays from 2014 October until 2015 May. The observational details and data reductions of the EDGE survey are presented in Bolatto et al. (2017). Briefly, the EDGE sample galaxies are selected from the CALIFA Second Data Release (García-Benito et al. 2015) based on their fluxes in the WISE 22μm band (Wright et al. 2010). The raw data are reduced using the `MIRIAD` package (Sault et al. 1995) into data cubes, i.e. CO intensity as a function of velocity, right ascension, and declination.

The beam size for each galaxy varies with a typical value of $4''.5$, which corresponds to a median physical scale of about 1.5 kpc. This physical resolution is slightly larger than previous CO surveys, such as BIMA SONG ($\sim$ 360 pc; Helfer et al. 2003), HERACLES ($\sim$ 500 pc; Leroy et al. 2009), and STING (160 − 1250 pc; Rahman et al. 2012), because our sample covers farther median distance than those surveys. The velocity resolution is 10 km s^{-1} with a typical velocity range of 860 km s^{-1}. This velocity range generally covers CO emission out to the flat part of the rotation curve. Data cubes which provide an estimate of $1\sigma_{\rm rms}$ noise level at each pixel were also generated during the data reduction processes.

In order to separate signal from noise, we create masks through the following steps using `IDL` (code available at `https://github.com/tonywong94/idl_mommaps`; Wong et al. 2013). First, we smooth the data to $9''$ resolution using a Gaussian kernel. The aim of this smoothing is to reach a higher signal to noise ratio (SNR). Then, we search for contiguous regions, starting from pixels that have SNR ≥ 3.5 extending down to regions that have SNR $= 2$. The aim of contiguous regions is to exclude pixels that by chance have high flux due to noise, but only localized into one to few pixels (e.g., Rosolowsky & Leroy 2006). An additional padding of 2 pixels surrounding the $2\sigma_{\rm rms}$ contours are added into the mask to capture low level emission. Finally, we apply these masks to the data cubes in their original resolutions ($4''.5$ and 10 km/s). We define these contiguous regions, including the padding, as masked regions.

The masked data cubes are integrated along the velocity

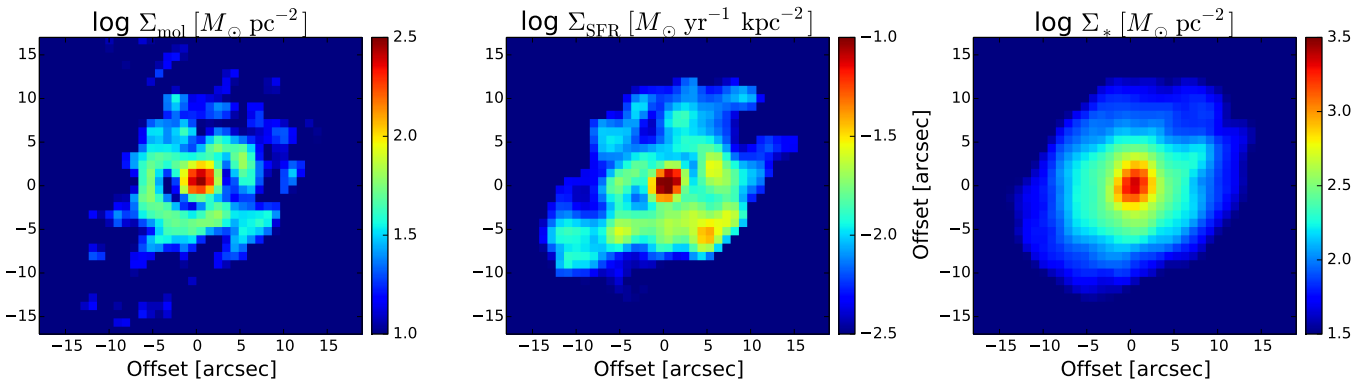

Figure 1. From left to right: the maps of stellar, molecular gas, and SFR surface density for NGC 2253.

axis to get the CO surface brightness maps (zeroth moment maps). Similarly, the uncertainties of the maps are derived by integrating the estimated noise along the velocity axis within the masked cubes. In the analyses, we use these uncertainty maps as $1\sigma_{\rm rms}$ noise level. Note that not all masked CO surface brightness maps are higher than $2\sigma_{\rm rms}$ level, therefore, we treat emission below $2\sigma_{\rm rms}$ level as non-detection, even though these emissions are located within the mask.

We convert the CO surface brightness and its uncertainty maps into molecular gas surface density ($\Sigma_{\rm mol}$) maps by using a constant CO-to-H_2 conversion factor ($\alpha_{\rm CO}$) of 4.4 $M_\odot$ pc^{-2} (K km s^{-1} pc^2)$^{-1}$, including the mass contribution from helium. In general, $\alpha_{\rm CO}$ can vary as a function of metallicity and stellar surface density (Bolatto et al. 2013). In our approach, we assume a Galactic value of $\alpha_{\rm CO}$, and then, we consider how the variations in $\alpha_{\rm CO}$ affect our results. Note that the surface density measurement has been corrected (deprojected) for inclination (i) by using a correction factor of cos(i). An example map of $\Sigma_{\rm mol}$ is shown as the first column of Figure 1.

2.2. *The CALIFA Survey*

CALIFA is an optical Integral Field Unit (IFU) survey of $\sim$ 600 local galaxies in a redshift (z) range of $0.005 \lesssim z \lesssim 0.03$ using the 3.5-m telescope at the Calar-Alto observatory (Sánchez et al. 2012). The CALIFA samples are selected from the SDSS DR7 database (Abazajian et al. 2009) based on their diameter in $r-$band ($45'' < D_{25} < 80''$), so that they fit well within the IFU field-of-view of $1'.3$, or equivalently $\sim$ 2.5 effective radius (Walcher et al. 2014), but statistically still represents the population of $z \sim 0$ galaxies in the color-magnitude diagram. In an IFU survey, we get spatial and spectral information of an object, simultaneously. The spatial resolution of CALIFA is $\sim 2''.5$ (or $\sim$ 1 kpc) and the spectral range of CALIFA covers 3700 to 7000 Å, so that it captures the stellar absorption lines and the nebular emission lines.

We do the following additional processes to create homogeneous datasets for comparing EDGE and CALIFA. (1) Regrid the CALIFA data by using `MIRIAD` task `regrid`, so that it has the same spatial coordinate as in the EDGE data with a common pixel size of $2'' \times 2''$. In this process, we also degrade the resolution of CALIFA images to match the resolution of EDGE images by using `MIRIAD` task `convol`. The total flux is conserved during those processes. (2) Blanking the CALIFA data that are contaminated by foreground stars and neighboring galaxies. (3) Separating signals from noise by blanking any pixels that have SNR < 2, where we use the median-absolute-deviation of the CALIFA image as an estimate of the noise.

The physical resolution from galaxy-to-galaxy varies between $\sim$ 0.5 to 2 kpc. However, we do not expect that these variations affect our results because Schruba et al. (2010) and Kruijssen & Longmore (2014) concluded that the locations of CO and Hα peak are co-spatial on scales larger than $\sim$ 0.5 kpc, i.e. we only capture the time-average of the star formation process, not its time evolution. In addition, degrading all samples to a resolution of 2 kpc is not suitable for studying the variation of $\tau_{\rm dep}$ in the central part of galaxies ($r < 2$ kpc) versus the galaxy disks. Conversely, only a small fraction of galaxy sample has resolution of $\sim$ 0.5 kpc.

2.2.1. *The Star Formation Rate Surface Density*

Post-processing of CALIFA data (`Pipe3D` version 2.2 from Sánchez et al. 2016) provides the intensity maps of emission lines, such as Hα and Hβ. To derive maps of the SFR surface density ($\Sigma_{\rm SFR}$), first, we calculate the nebular extinction at Hα ($A_{\rm H\alpha}$), by utilizing the ratio of Hα and Hβ fluxes (Balmer decrement method; e.g., Domínguez et al. 2013) and compare it with its intrinsic value (zero extinction) of 2.86 (for case B recombination at temperature of 10^4 K and electron density of 100 cm^{-3}; Osterbrock 1989). We also use a Galactic extinction curve (Cardelli et al. 1989) with $R_V = 3.1$. The result would be similar if we used Calzetti et al. (2000) extinction curve with $R_V = 4.1$, because $A_{\rm H\alpha,Calzetti}/A_{\rm H\alpha,Cardelli} = 1.03$ (Catalán-Torrecilla et al. 2015). The resulting pixel-by-pixel mean value of $A_{\rm H\alpha}$ is $\sim$ 1 magnitude.

Then, we apply this $A_{\rm H\alpha}$ to Hα maps to get the *dust-corrected* (or extinction-free) Hα maps. An example of this Balmer decrement method is shown in Figure 2. Finally, we convert the dust-corrected Hα maps to the SFR surface density maps following the prescriptions in Calzetti et al. (2007), based on a stellar population model with 100 Myr of constant SFR, solar metallicity, and an IMF that has a slope of -1.3

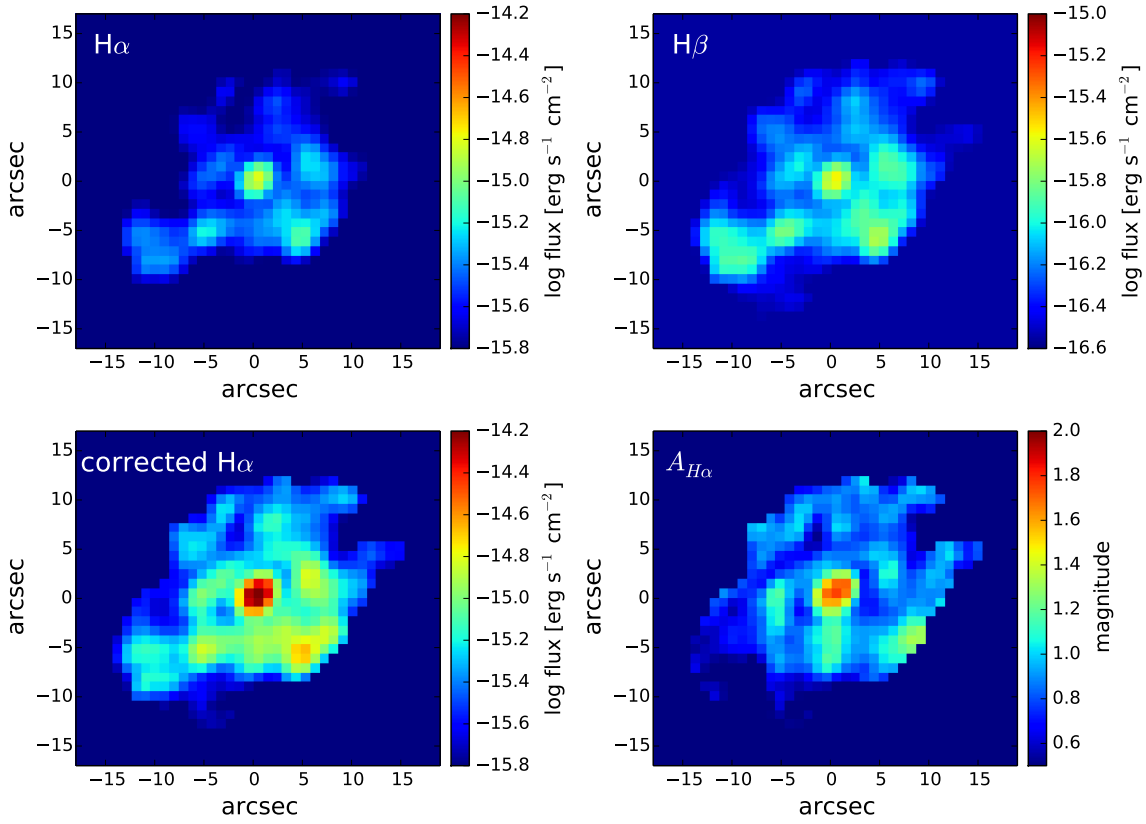

Figure 2. An application of the Balmer decrement method to NGC 2253. Top left: Hα fluxes. Top right: Hβ fluxes. Bottom right: Dust extinction at Hα ($A_{H\alpha}$). Bottom left: Extinction corrected Hα fluxes.

within $0.1 < M_*/M_\odot < 0.5$ and a slope of -2.3 within $0.5 < M_*/M_\odot < 120$. The IMF for this SFR prescription is similar to a Kroupa (2001) IMF, which is a factor of 1.59 smaller than those derived from a Salpeter (1955) IMF with a mass range of $0.1-100\ M_\odot$ (Madau & Dickinson 2014). An example of the $\Sigma_{\rm SFR}$ maps is shown as the second column of Figure 1.

As a check, we compare the SFR of *extinction-corrected* Hα emission that we derived above with the SFR derived from the ultraviolet (UV) emission plus total-infrared (TIR) emission from Catalán-Torrecilla et al. (2015). The UV emission traces the unobscured SFR, while the TIR emission compensates for the obscured SFR that is reradiated by dust. We do galaxy-by-galaxy comparison by integrating our resolved SFR because the IR data is unresolved. Since the Hα emission is more extended than the FoV of CALIFA survey, we apply an aperture correction of 1.4 as suggested by Catalán-Torrecilla et al. (2015). In Figure 3, we show that both measurements are in agreement within a factor of ~ 2.

2.2.2. *The Gas-phase Metallicites*

We determine the gas-phase metallicities by using emission line ratios of OIII[5007Å]/Hβ and NII[6583Å]/Hα (i.e. the O3N2 method; Alloin et al. 1979; Pettini & Pagel 2004). We use the following prescription from Marino et al. (2013)

$$12 + \log({\rm O/H}) = 8.533 - 0.214 \log\left(\frac{\rm OIII}{\rm H\beta}\frac{\rm H\alpha}{\rm NII}\right). \quad (1)$$

The coefficient of this method has been calibrated by using the electron temperature based measurements of 603 HII regions extracted from the literature and 3423 additional HII complexes from the CALIFA survey. The resolved metallicities in our sample range from 8.3 to 8.6, slightly below the Solar metallicity of 8.7 (Allende Prieto et al. 2001).

2.2.3. *The Stellar Ages and Mass Surface Densities*

We take the luminosity-weighted, stellar population ages and the dust-corrected, stellar mass surface densities (Σ_*) from the data products of `Pipe3D` version 2.2 (Sánchez et al. 2016). Briefly, the data products are derived from the best fit of stellar spectrum from a combination of the GRANADA (Martins et al. 2005) and MILES libraries (Sánchez-Blázquez et al. 2006; Vazdekis et al. 2010; Falcón-Barroso et al. 2011), that cover 39 grids of stellar ages (from 1 Myr to 13 Gyrs) and 4 grids of stellar metallicities ($Z/Z_\odot = 0.2, 0.4, 1$ and 1.5). We convert the Σ_* maps from a Salpeter (1955) IMF to a Kroupa (2001) IMF by divide it with a factor of 1.6 (Madau & Dickinson 2014).

3. SAMPLE SELECTION

We select 52 galaxies from 126 EDGE-CALIFA samples based on the following three criteria. (1) They are not dominated by AGN/LINER. (2) They have sufficient SFR and CO detections that cover both the center of a galaxy and its disk. (3) The inclination (i) is less than 75°. The inclinations are

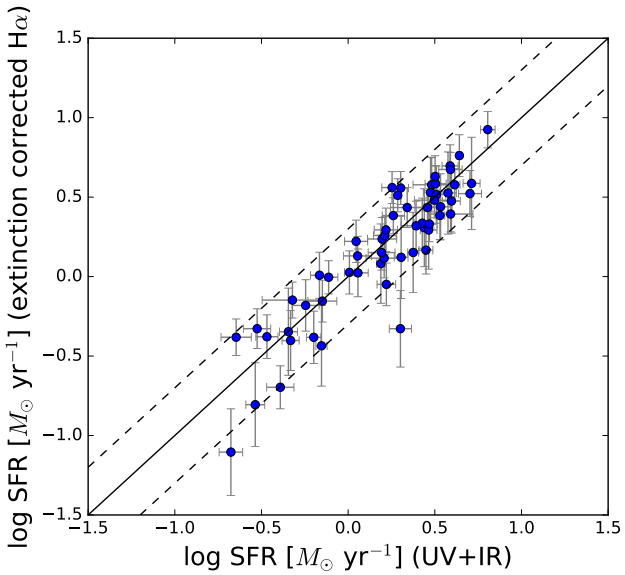

Figure 3. A comparison of SFR measurements from extinction-corrected Hα (this paper) and UV+IR from Catalán-Torrecilla et al. (2015). We apply aperture correction for our SFR measurement as suggested by Catalán-Torrecilla et al. (2015). The solid line is the one-to-one relationship, while the dashed line is 0.3 dex away from the solid line. The uncertainties of SFR measurement in this paper is calculated using the error propagation from the uncertainties in Hα and Hβ measurements. A 20% uncertainty due to SFR calibration (Calzetti et al. 2007) has been included.

taken from the following, ordered by priority: (1) the best fit of CO rotation curve, whenever it is possible (Levy et al. in preparation), (2) from the shape of the outer isophote, or (3) from the HyperLEDA catalog (Makarov et al. 2014). A list of the galaxy sample is tabulated in Table 1 in Appendix.

We exclude AGN and LINER emission regions based on N[II]/Hα and O[III]/Hβ line ratios (i.e. the BPT diagram; Baldwin et al. 1981; Kewley & Dopita 2002; Kauffmann et al. 2003). Any data points above the demarcation line of Kewley & Dopita (2002) are blanked. Note that the LINER emission regions are not only concentrated in the center, but also in the disk, possibly due to photo-ionization from AGB stars (Singh et al. 2013; Belfiore et al. 2016). A galaxy is removed from the sample if all pixels in the center (i.e. within $0.1\ R_{25}$) are AGN/LINER-like emission. Based on the criteria above, 31 galaxies are removed from the sample. We also blanked any regions that have Hα equivalent width less than 6 Å, because $\sim 80\%$ of stars in those regions are older than ~ 500 Myrs, and hence, not associated to star forming regions (Sánchez et al. 2014).

We further remove 17 galaxies that do not have sufficient CO or SFR detection in their center or disk, because measurement of $\tau_{\rm dep}$ is severely contaminated by non-detection. If a galaxy has less than 2 detected pixels in the center or in the disk, then that galaxy is removed from the sample. Lastly, 26 galaxies with $i \gtrsim 75^\circ$ (the ratio of minor to major axis is less than 0.25) are removed because high inclination galaxies yield few sampling points along the minor axis, resulting in a deprojected beam elongated parallel to the minor axis in the plane of the galaxy, and large uncertainty in the estimation of dust extinction.

Our final sample has stellar masses (M_*) from 4×10^9 to $2 \times 10^{11}\ M_\odot$, molecular gas masses ($M_{\rm mol}$) from 8×10^7 to $1 \times 10^{10}\ M_\odot$, and gas-phase metallicities (12+log[O/H]) from 8.4 to 8.6. Our sample consists of 49 spirals (Hubble type from Sa to Sd) and 3 early-types, including 24 barred galaxies (Méndez-Abreu et al. 2017) and 7 interacting galaxies (Barrera-Ballesteros et al. 2015). The ranges in the stellar and molecular gas masses are comparable to the unresolved survey of COLDGASS (Saintonge et al. 2011a,b). In addition, we have a comparable number of galaxies and cover farther distance (d) in the local volume ($26 \lesssim d \lesssim 169$ Mpc) than previous resolved surveys, such as BIMA SONG (44 galaxies; $2 \lesssim d \lesssim 26$ Mpc; Helfer et al. 2003), HERACLES (48 galaxies; $3 \lesssim d \lesssim 15$ Mpc; Leroy et al. 2013; Schruba et al. 2012), and CARMA STING (14 galaxies; $5 \lesssim d \lesssim 43$ Mpc; Rahman et al. 2012). Thus, our sample bridges the gap between nearby and higher redshift galaxies.

4. RESULTS

In Figure 4, we show the KS relation for molecular gas. The data points are from pixel measurements (detected both in SFR and CO) in 52 galaxies. The median values of $\Sigma_{\rm SFR}$ for a given bin of $\Sigma_{\rm mol}$ are marked as black dots, while the constant values of $\tau_{\rm dep}$ = 1, 2, and 4 Gyrs are indicated. There is a tendency for high $\Sigma_{\rm mol}$ regions (top right in Figure 4) to have shorter $\tau_{\rm dep}$ than low $\Sigma_{\rm mol}$ regions. Since galactic centers have higher $\Sigma_{\rm mol}$ than those in the disks, this indicates that the centers have shorter $\tau_{\rm dep}$ than those in the disks.

In order to study the variation of $\tau_{\rm dep}$ between galactic centers and disks, we first need to separate the center of a galaxy from its disk. To do so, we define the center as a region at distance $r \leq 0.1\ R_{25}$ from the galactic nucleus, and the disk as a region between $0.1\ R_{25}$ and $0.7\ R_{25}$. We define $\tau_{\rm center}$ ($\tau_{\rm disk}$) as the median of $\tau_{\rm dep}$ over all detected pixels in the center (disk). If the median of $\tau_{\rm dep}$ in a galaxy is used ($\tau_{\rm median}$), it means we cover both the center and the disk. If the number of detected pixels in the disks is much larger than those in the centers, then the values of $\tau_{\rm median}$ is similar to $\tau_{\rm disk}$. We adopt $r = 0.7\ R_{25}$ as the outermost radius because CO is hardly detected beyond that radius.

The radial distance to the galactic nucleus is calculated using the assumption that the molecular gas lies in the galactic mid-plane, without warp, isophotal twist, or misalignment. Since each galaxy has different physical size in kpc, we normalize the radius with respect to R_{25}, i.e. the radius where the surface brightness is 25 mag/arcsec^2 in the $B-$band. We adopt the values of R_{25} from the HyperLEDA catalog. The conversion between R_{25} and the stellar scale length (l_*) is $R_{25} = (4.6 \pm 0.8)\ l_*$ (Leroy et al. 2008). Unless otherwise stated, throughout this paper we focus on pixels detected in both CO ($\Sigma_{\rm mol} \gtrsim 10\ M_\odot$ pc^{-2}) and Hα, corresponding to $\sim$kpc scale regions of star formation. It should be noted that typically there are approximately four pixels per synthesized beam area.

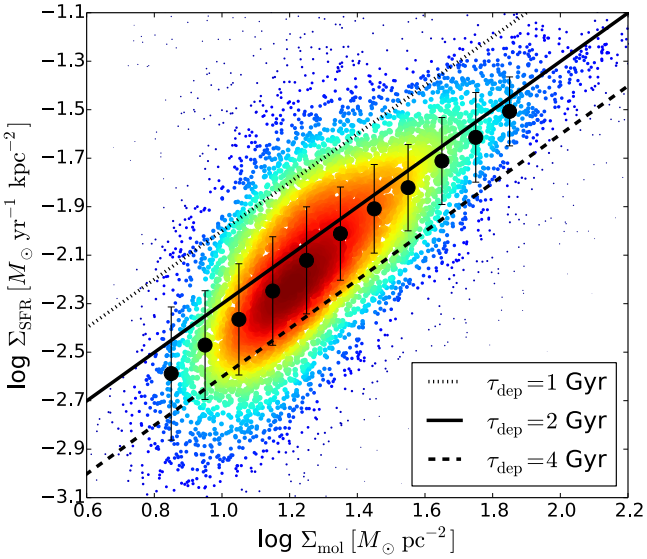

Figure 4. The relationship between $\Sigma_{\rm mol}$ and $\Sigma_{\rm SFR}$ for our sample of 52 galaxies selected from the EDGE survey. The data point plots these values for a $2'' \times 2''$ pixel, with color and point size are coded by the density of data points. The black dots are the median value of $\Sigma_{\rm SFR}$ within bins of $\Sigma_{\rm mol}$. The dotted, solid, and dashed lines correspond to $\tau_{\rm dep}$ = 1, 2, and 4 Gyrs, respectively.

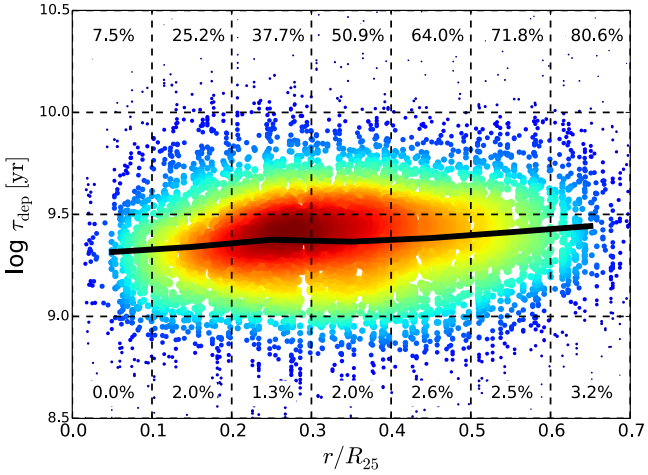

Figure 5. The depletion time as a function of radius, stacked over all detected regions in each sample galaxy. The data points are $2'' \times 2''$ pixel measurements. The colors and sizes of points represent the global density of the data points and the solid line is the median value of $\tau_{\rm dep}$ in a radial bin. On the top and bottom of the figure, we label the fractions of non-detection pixels that correspond to upper and lower limits in $\tau_{\rm dep}$, respectively. Upper limits in $\tau_{\rm dep}$ are pixels with known SFR but CO is not detected, and vice versa for lower limits. The Hα measurements are more sensitive than the CO maps, therefore, the fractions of upper limits are higher than the fractions of lower limits at any radius.

4.1. *Variations of the Molecular Gas Depletion Time*

Since CO emission is patchy, not all regions within a galaxy are detected in both CO and Hα. To investigate $\tau_{\rm dep}$ as a function of radius, we stack the pixels from all galaxies in all sample. In Figure 5, $\tau_{\rm dep}$ for each pixel detected in both CO and Hα is plotted as a function of radius (r/R_{25}). The median value of $\tau_{\rm dep}$ is 2.4 Gyrs with ~ 0.5 dex scatter. This value is in line with previous measurements in nearby galaxies (e.g., Rahman et al. 2012; Bigiel et al. 2011; Leroy et al. 2013). However, Figure 5 shows that centers have shorter $\tau_{\rm dep}$ than those in the disks. The dip of $\tau_{\rm dep}$ in the centers is seen in some of our galaxies but not all. The dip of $\tau_{\rm dep}$ becomes more prominent when we separate those galaxies from the rest of the sample (see §4.2).

To investigate variations in $\tau_{\rm dep}$ between the center and the disk, we calculate the mean value of $\tau_{\rm dep}$ in the center and the disk for each galaxy separately, referring to these as $\tau_{\rm center}$ and $\tau_{\rm disk}$, respectively. The result is shown in Figure 6, where it can be seen that $\tau_{\rm center}$ is an order of magnitude shorter than $\tau_{\rm disk}$ in some galaxies, and an order of magnitude higher than $\tau_{\rm disk}$ in other galaxies.

We investigate whether the variations of $\tau_{\rm center}$, relative to $\tau_{\rm disk}$, are correlated with the global properties of galaxies, namely the stellar masses (M_*), the molecular gas masses ($M_{\rm mol}$), the Hubble types, the gas-phase metallicities, and the age of stellar populations. We adopt RC3 de Vaucouleurs et al. (1991) indices from the HyperLEDA database (Makarov et al. 2014) as morphological types. For the oxygen abundance and the age of stellar population, we use their median value within 1 ± 0.2 effective radius (R_e) because Sánchez et al. (2016) suggest that the value at R_e is a good representation in a galaxy.

We do not find correlations between $\log(\tau_{\rm center}/\tau_{\rm disk})$ and morphology, gas-phase metallicity, or age of stellar populations at R_e, probably because we have limited range in morphology (94% of our samples are spirals) and gas phase metallicity (only ~ 0.2 dex of variations). Furthermore, the age of stellar populations at R_e reflect the value in the disks, where $\tau_{\rm disk}$ does not vary as much as $\tau_{\rm center}$. If we measure the stellar age in the center, however, galaxies with low values of $\log(\tau_{\rm center}/\tau_{\rm disk})$ have younger ages for their stellar populations (see §5.3).

Furthermore, $\log(\tau_{\rm center}/\tau_{\rm disk})$ is correlated with $M_{\rm mol}/M_*$, but we find no significant correlation with $M_{\rm mol}$, and no correlation with M_* (Figure 6). Galaxies with shorter $\tau_{\rm center}$ than $\tau_{\rm disk}$ have lower fraction of molecular gas to stellar mass. The physical reason for this correlation is unknown. Sandstrom et al. (2013) found that the CO-to-H_2 conversion factor ($\alpha_{\rm CO}$) is lower in galactic centers. If we apply this variation to our sample, it makes the difference between $\tau_{\rm center}$ and $\tau_{\rm disk}$ is even larger.

It should be noted that three galaxies with the lowest values of $\log(\tau_{\rm center}/\tau_{\rm disk})$ are interacting galaxies (marked as black squares in Figure 6). In addition, barred galaxies (identified from the photometric fit of Méndez-Abreu et al. 2017, or from HyperLEDA catalog) tend to have lower values of $\log(\tau_{\rm center}/\tau_{\rm disk})$ than unbarred galaxies (marked as black diamonds in Figure 6). The mean values of $\log(\tau_{\rm center}/\tau_{\rm disk})$ for interacting and barred galaxies are -0.42 ± 0.51 and -0.22 ± 0.28, while the corresponding value for unbarred galaxies is -0.03 ± 0.35. This indicates that perturbed systems can enhance the star formation efficiency in the center.

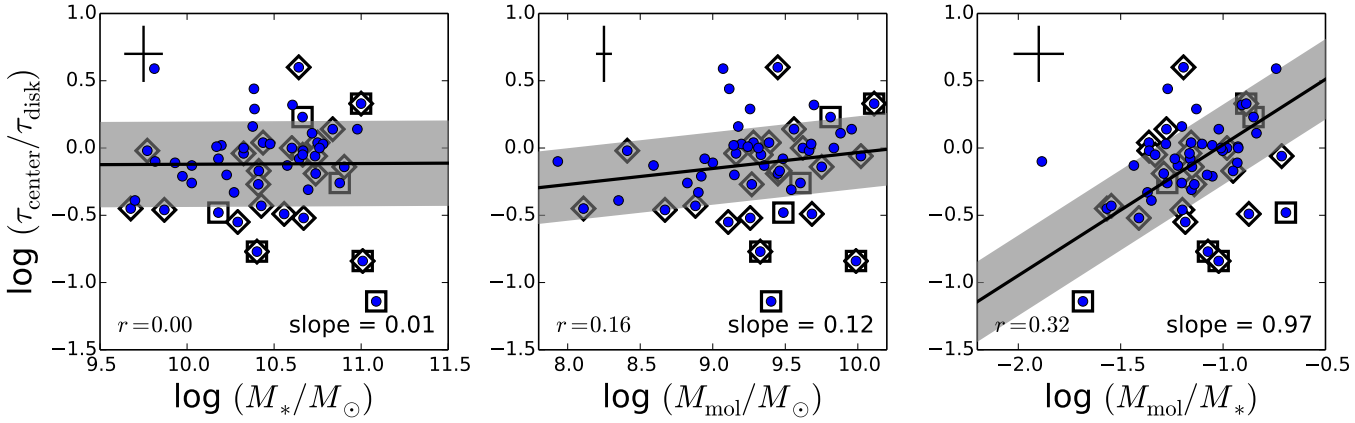

Figure 6. The ratio of $\tau_{\rm dep}$ in a galactic center to that in its disk for each galaxy is plotted as a function of various global parameters: stellar masses (left panel), molecular gas masses (middle panel), molecular-to-stellar mass ratio (right panel). The diamonds mark the barred galaxies, while the squares mark the interacting galaxies. The black lines are the linear best-fit using Orthogonal Distance Regression method in `Scipy` package, which takes into account the errors in both axes, and the gray regions cover 68% of the nearest data points to the best-fit lines. The slope of the best-fit line and the Pearson correlation coefficient are indicated. The crosses represent the typical error bars of the data points.

4.2. *Separations of Galaxies into Three Groups of* $\tau_{\rm dep}$

To see clear variations of $\tau_{\rm center}$ with respect to $\tau_{\rm disk}$, we separate galaxies into three groups based on their $\log(\tau_{\rm center}/\tau_{\rm median})$ values. The three groups of $\tau_{\rm dep}$ are the following. (1) Galaxies with falling $\tau_{\rm center}$, defined as those with $\log(\tau_{\rm center}/\tau_{\rm median}) < -0.26$ dex, which represent 25.0% of the galaxy sample. (2) Galaxies with rising $\tau_{\rm center}$, defined as those with $\log(\tau_{\rm center}/\tau_{\rm median}) > 0.26$ dex, which represent 9.6% of the galaxy sample. (3) The rest of them (65.4% of the sample) have $\log(\tau_{\rm center}/\tau_{\rm median})$ within ± 0.26 dex, which we defined as flat $\tau_{\rm dep}$. We list the values of $\tau_{\rm dep}$ in the centers, disks, and whole galaxy (median) in Table 1, where we use the notation "drop", "rise", and "flat" for these three groups. In this respect, we expand the previous finding by Leroy et al. (2013) to include the galactic centers that have similar, and even, longer $\tau_{\rm center}$ compared to $\tau_{\rm median}$. The results of this segregation are shown in the top row of Figure 7.

We use 0.26 dex as a separator between the three different groups of $\tau_{\rm dep}$ because this value is the standard deviation of resolved $\tau_{\rm dep}$ within 0.7 R_{25}. This value also coincides with that seen in the HERACLES sample, which shows a dip of $\tau_{\rm center}$ by about 0.2 dex relative to $\tau_{\rm median}$ (for a constant CO-to-H_2 conversion factor; Leroy et al. 2013). However, keep in mind that the variation of $\tau_{\rm center}$ is continuous, i.e. there is no clear separation or clustering between those three groups (see Figure 6). The classification of galaxies into three groups is just an approach to see a difference between $\tau_{\rm center}$ and $\tau_{\rm median}$ in some galaxies.

In the bottom row of Figure 7, we show each of the three groups on an absolute scale of $\tau_{\rm dep}$ (in years). It shows that the galactic centers in the drop (rise) $\tau_{\rm center}$ groups form stars more (less) efficiently than those in the flat $\tau_{\rm dep}$ group, i.e. their locations in the KS diagram lie above (below) the disks. The values of $\tau_{\rm center}$ in the drop $\tau_{\rm dep}$ group ($\approx$ 1 Gyr) are not only lower relative to $\tau_{\rm median}$, but also in the absolute value, because $\tau_{\rm median} \approx 2.4$ Gyr. Therefore, those galactic centers resemble an intermediate regime between the disks and starbursts.

4.3. *The Local Properties*

Is the variation of $\tau_{\rm dep}$ between the centers and the disks correlated with $\Sigma_{\rm SFR}$, $\Sigma_{\rm mol}$, or both? In Figure 8, we show that there is an anti-correlation between $\log(\tau_{\rm center}/\tau_{\rm disk})$ and $\log(\Sigma^{\rm center}_{\rm SFR}/\Sigma^{\rm disk}_{\rm SFR})$, but no correlation between $\log(\tau_{\rm center}/\tau_{\rm disk})$ and $\log(\Sigma^{\rm center}_{\rm mol}/\Sigma^{\rm disk}_{\rm mol})$. This means the drop of $\tau_{\rm center}$ is due to higher $\Sigma_{\rm SFR}$, not lower $\Sigma_{\rm mol}$ in the center. In other words, the centers can have any values of $\Sigma_{\rm mol}$, but those with higher $\Sigma_{\rm SFR}$ are associated with the drops of $\tau_{\rm center}$. However, we should be cautious because the range of $\Sigma_{\rm mol}$ variations ($\sim$ 1 dex) is smaller than the range of $\Sigma_{\rm SFR}$ variations ($\sim$ 2 dex).

Why do some centers have higher $\Sigma_{\rm SFR}$, irrespective of the $\Sigma_{\rm mol}$ value? In thermal and dynamical equilibrium, the weight of the ISM in the vertical gravitational field of stars and gas is balanced by the pressure created by momentum and energy from stellar feedback (Ostriker et al. 2010; Ostriker & Shetty 2011; Kim et al. 2011, 2013). Therefore, we expect a relation between $\Sigma_{\rm SFR}$ (which sets the thermal, turbulent, and magnetic pressure via feedback) and Σ_* (which sets the ISM weight). Interestingly, in the right panels of Figure 8 we see that $\log(\tau_{\rm center}/\tau_{\rm disk})$ correlates with the ratio of the mean values of Σ_* between the center and the disk. Galaxies with higher ratio of central Σ_* relative to those in the disks, have a drop of $\tau_{\rm center}$. Since Σ_* is a proxy for hydrostatic pressure (Blitz & Rosolowsky 2004, 2006), this means the drops of $\tau_{\rm center}$ are associated with high ISM pressure. Indeed, previous observations showed that the galactic center is a high pressure region (Spergel & Blitz 1992; Oka et al. 2001; Rosolowsky & Blitz 2005). This result suggests the star formation efficiency depends on the local environment within a galaxy.

5. DISCUSSION

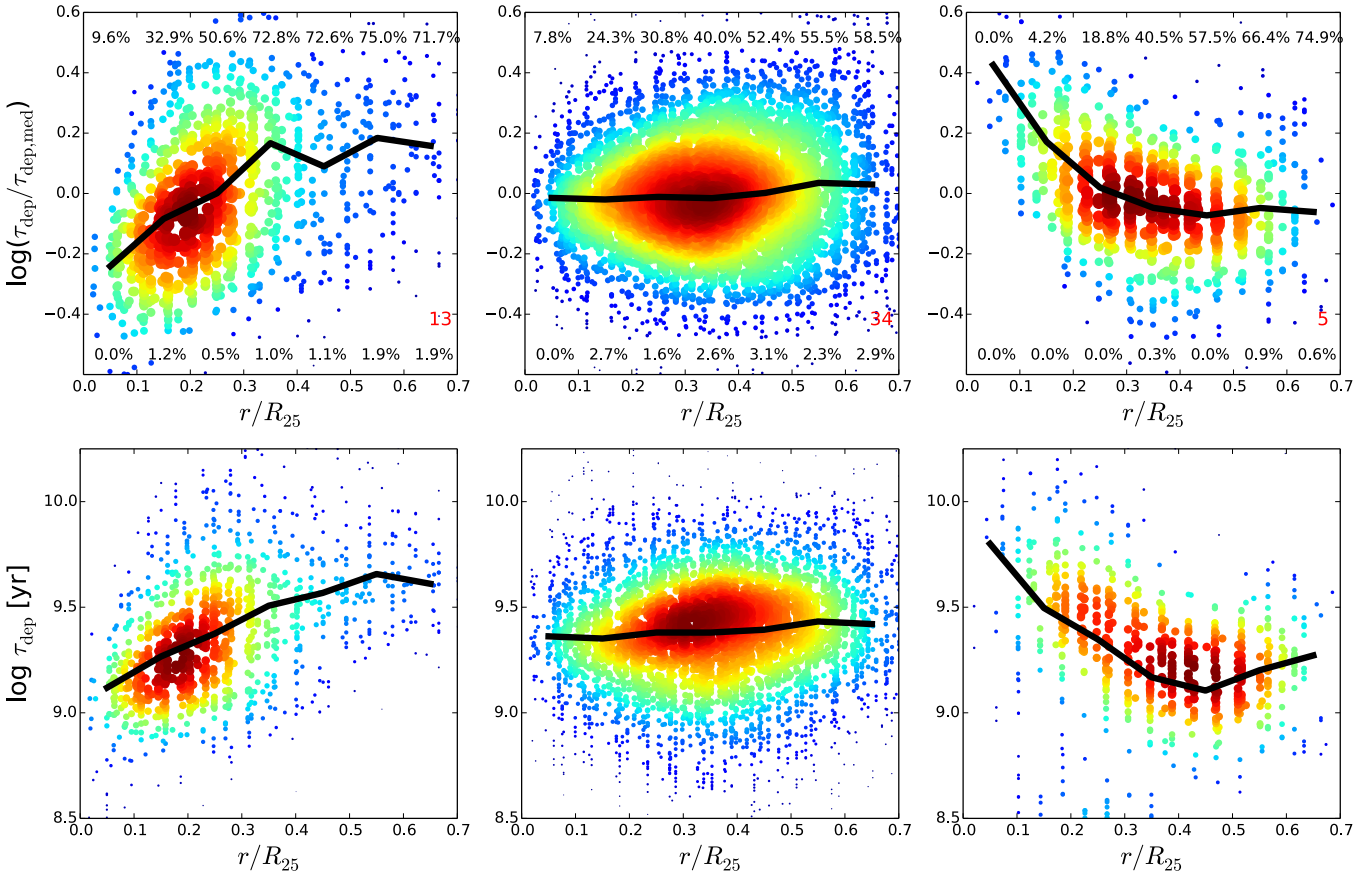

Figure 7. Classifications of $\tau_{\rm dep}$ over detected pixels: galaxies that show a drop of $\tau_{\rm dep}$ in the center (left), similar $\tau_{\rm dep}$ to the disk (middle), and longer $\tau_{\rm dep}$ in the center (right), in relative (top row) and absolute (bottom row) scales. The colors and sizes represent the density of data points. The median profiles for each groups are shown as black curves. The percentages on the top and bottom of top row are the fraction of non-detection, and the number of galaxies in each groups are stated in the bottom right corner of each top panels. This result extends the finding by Leroy et al. (2013), where we show more complex behaviors: galactic centers can have shorter, similar, or longer $\tau_{\rm dep}$ with respect to the disk.

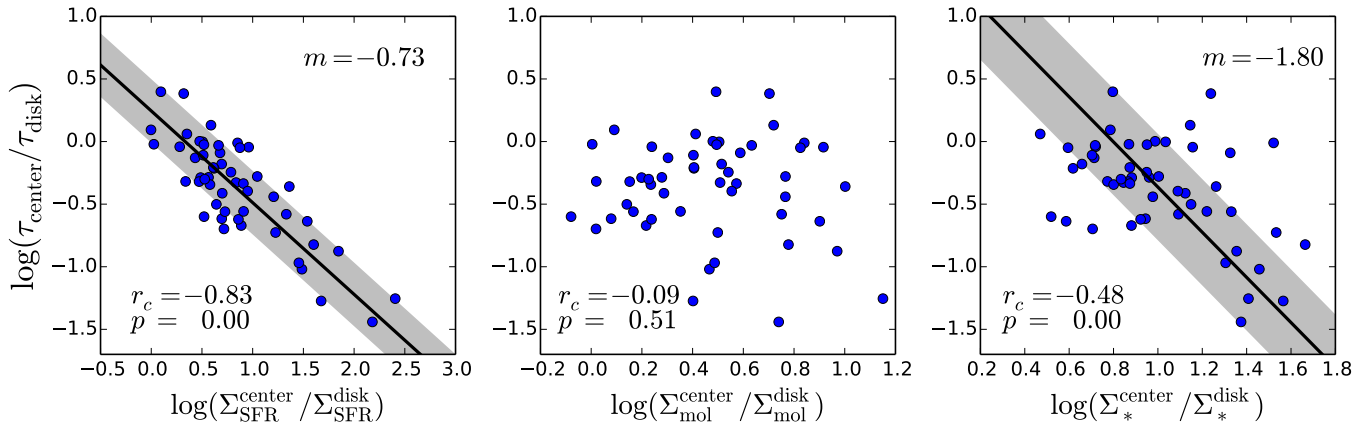

Figure 8. $\tau_{\rm center}$ relative to $\tau_{\rm disk}$ are plotted against Σ_*, $\Sigma_{\rm mol}$, and $\Sigma_{\rm SFR}$, averaged over detected regions in the center (left panel), the disk (middle panel), and the ratio between the two (right panel). The black lines are the linear fit with equal weight using orthogonal distance regression in `Scipy`, and the gray regions cover 68% of data points from the linear fit. The typical uncertainties of the data points are 4 $M_\odot$ pc^{-2} for Σ_* and $\Sigma_{\rm mol}$, and 10^{-4} $M_\odot$ yr^{-1} kpc^{-2} for $\Sigma_{\rm SFR}$. The slope of the correlation (m), the correlation coefficient (r_c), and the p-value (p) are indicated at the corner of each panels. We do not fit the middle panel because of low r_c and high p values, indicative of no correlation between $\log(\tau_{\rm center}/\tau_{\rm disk})$ and $\Sigma_{\rm mol}$.

5.1. *The CO-to-H_2 Conversion Factor*

How is the variation of $\tau_{\rm center}$ affected by the change in the CO-to-H_2 conversion factor ($\alpha_{\rm CO}$)? In general, there are two scenarios where $\alpha_{\rm CO}$ varies (Bolatto et al. 2013). First, the dependence of $\alpha_{\rm CO}$ on gas metallicity – a lower gas metallicity needs a higher H_2 column density to shield the gas until it reaches sufficient extinction for CO to exist (e.g., Leroy et al. 2007, 2011). However, the variation of metallicity from center to disk within a galaxy is very small (~ 0.1 dex; Figure 9), so that metallicity is unlikely to induce a significant variation in $\alpha_{\rm CO}$. Furthermore, in the group that shows a drop of $\tau_{\rm center}$, metallicities slightly rise towards the center, which means $\alpha_{\rm CO}$ is slightly lower in the center than in the disk. If we take this effect into account, it would only exaggerate the drop in $\tau_{\rm center}$.

The second source of $\alpha_{\rm CO}$ variations is the CO emission from diffuse gas that is bound by the gravitational potential of stars and gas. The velocity dispersion of this diffuse gas ($\sigma_{\rm CO,diff}$) reflects the additional stellar gravitational potential (Bolatto et al. 2013). This effect increases the CO luminosity ($L_{\rm CO}$) per unit molecular gas mass because $L_{\rm CO}$ is proportional to the brightness temperature (T_B) and $\sigma_{\rm CO,diff}$ (assuming CO is optically thick throughout the medium). Bolatto et al. (2013) and Sandstrom et al. (2013) suggest that the variation of $\alpha_{\rm CO}$ is related to the total surface density due to stars and gas as $\alpha_{\rm CO} \propto \Sigma_{\rm total}^{-\gamma}$, where $\gamma \approx 0.5$ for $\Sigma_{\rm total} > 100\ M_\odot\ {\rm pc}^{-2}$. Applying this prescription for $\alpha_{\rm CO}$ would exaggerate the drop in $\tau_{\rm center}$ and result in more galaxies in the group of $\tau_{\rm center}$ drops.

5.2. *Metallicity Gradients*

It is interesting that the metallicity in the drop $\tau_{\rm center}$ group rises toward the centers, while the metallacity profiles in the other two groups are flatten toward the centers (Figure 9). In the CALIFA sample, Sánchez-Menguiano et al. (2016) found the variation of metallicity gradients for different stellar masses: the metallicity gradient in higher mass galaxies is flattening in the center, while the metallicity gradient in lower mass galaxies is rising toward the center. Since the drop of $\tau_{\rm dep}$ is more prominent in the lowest mass bin (Figure 10), the variation of metallicity gradients in Figure 9 is possibly driven by their correlation with stellar masses. However, it remains unknown why the metallicity gradient depends on the stellar masses.

An alternative interpretation of steeper metallicity gradient is an enhancement of SFR per unit gas mass in the center (i.e. a low value of $\tau_{\rm center}$) leads to more metal enrichment than in the disk. Unlike stellar metallicity, gas-phase metallicity is more sensitive to the recent star formation, and hence, reflects the current value of $\tau_{\rm center}$. However, the center is not a closed-box system because of inflowing gas from the disk and outflowing gas driven by the stellar feedback. Furthermore, the gas-phase metallicity is also determined by the star formation history, not only the current star formation. Therefore, the rising gradient of metallicity in the short $\tau_{\rm center}$ group is not clearly understood.

5.3. *The Size of Molecular Disk*

In Figure 7, we see that the distribution of data points in the short $\tau_{\rm center}$ group is more concentrated toward the center, compared to those in the flat $\tau_{\rm dep}$ group. This gives a clue that the size of molecular disk in the short $\tau_{\rm center}$ group may be smaller (more compact). In order to quantify the compactness of the molecular gas and stellar distribution, we calculate the half-mass radius of molecular gas ($R_{50}^{\rm mol}$) and stars (R_{50}^{*}) from the cumulative distribution of $\Sigma_{\rm mol}$ and Σ_{*} as a function of radius.

In Figure 11, we plot $\log(\tau_{\rm center}/\tau_{\rm disk})$ against $R_{50}^{\rm mol}$ and R_{50}^{*}. It turns out that galaxies in the drop $\tau_{\rm center}$ group have smaller $R_{50}^{\rm mol}$ and R_{50}^{*} than those in the other groups. Furthermore, the disturbed systems (barred and interacting galaxies) tend to have smaller $R_{50}^{\rm mol}$ than unbarred, isolated galaxies. About 75% of galaxies in the drop $\tau_{\rm center}$ group are disturbed system, compared to only 44% and 40% for the flat $\tau_{\rm dep}$ and the rise $\tau_{\rm center}$ group, respectively. This gives a clue that the driver of physical size of the stellar and molecular gas distribution (e.g. bar and interactions) is linked to the cause of $\tau_{\rm dep}$ variation in the centers. We suspect that the bar drives the gas inward toward the center (or in the case of interacting galaxies, the gas lose its angular momentum). This radial gas compression increase the pressure, and resulting in higher star formation efficiency in the galactic center.

5.4. *A Burst of Star Formation*

There may be a central starburst activity on scales below our resolution, as indicated by the stellar population ages. There are at least two tracers of the stellar population ages: the UV-to-Hα ratio (e.g., Leroy et al. 2012; Weisz et al. 2012) and the age derived from the stellar population synthesis (which is available in the IFU data products of Sánchez et al. 2016). Since we do not have the resolved UV maps in hand, we can only rely on the second tracer. In Figure 12, we show the histogram of the luminosity-weighted ages of stellar populations in the centers ($r < 0.1\ R_{25}$) for each $\tau_{\rm dep}$ groups. It turns out that the centers in the drop $\tau_{\rm center}$ group (left panel) tend to have younger ages of stellar populations (≈ 2.1 Gyrs) than the other two groups (≈ 2.5 and ≈ 3.1 Gyrs; middle and right panels). This strengthens our suspicion that the centers of the short $\tau_{\rm center}$ group currently are undergoing a burst of star formation. However, further high resolution data are needed to confirm it.

6. SUMMARY

We present results from the EDGE survey, a spatially resolved CO follow-up to an IFU survey of local galaxies (CALIFA). We combine the CO and optical IFU data to study the variation of $\tau_{\rm dep}$ between the centers and the disks in 52 local galaxies. Our findings are the following.

1. Galactic centers can have shorter, longer, or similar $\tau_{\rm dep}$ compared to the disks (Figure 7), extending the previous result by Leroy et al. (2013). The short $\tau_{\rm center}$ group (representing 25% of the samples with $\tau_{\rm center}$ $\sim$ 1 Gyr) resembles the intermediate regime between the disks ($\tau_{\rm disk} \sim 2.4$ Gyrs) and starbursts ($\tau_{\rm dep} \sim 0.2$ Gyrs). Applying the decrease in CO-to-H_2 conversion

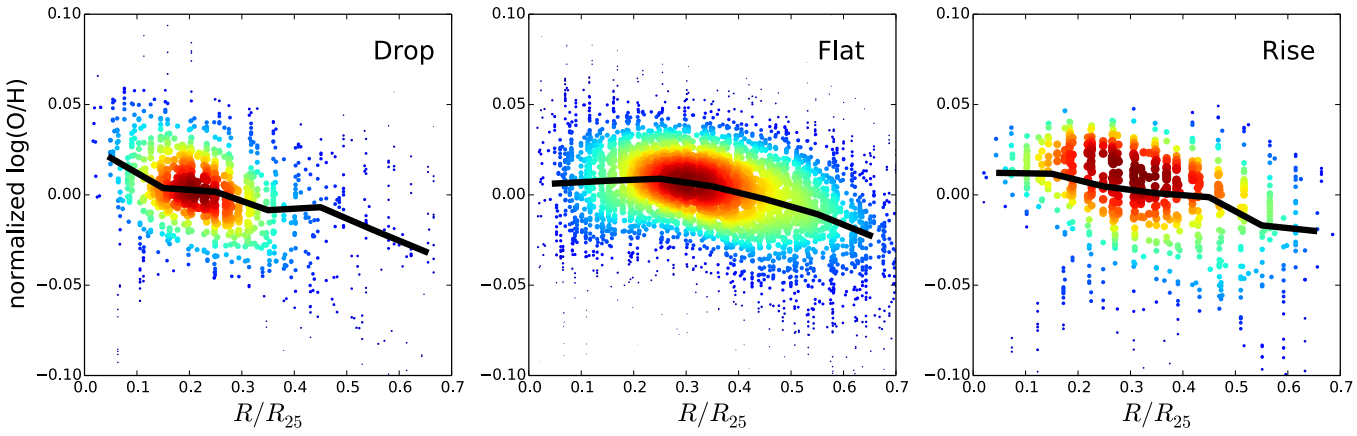

Figure 9. Plots of the gas-phase metallicities (12+log[O/H]), relative to their median value in a galaxy, as a function of radius for the three groups: drop of $\tau_{\rm center}$ (left), flat $\tau_{\rm dep}$ (middle), and rise of $\tau_{\rm center}$ (right). The median values are shown as the solid black curves and the colors represent the density of data points. The galaxies that show drops of $\tau_{\rm center}$ have steeper gradient of metallicity than the other two groups.

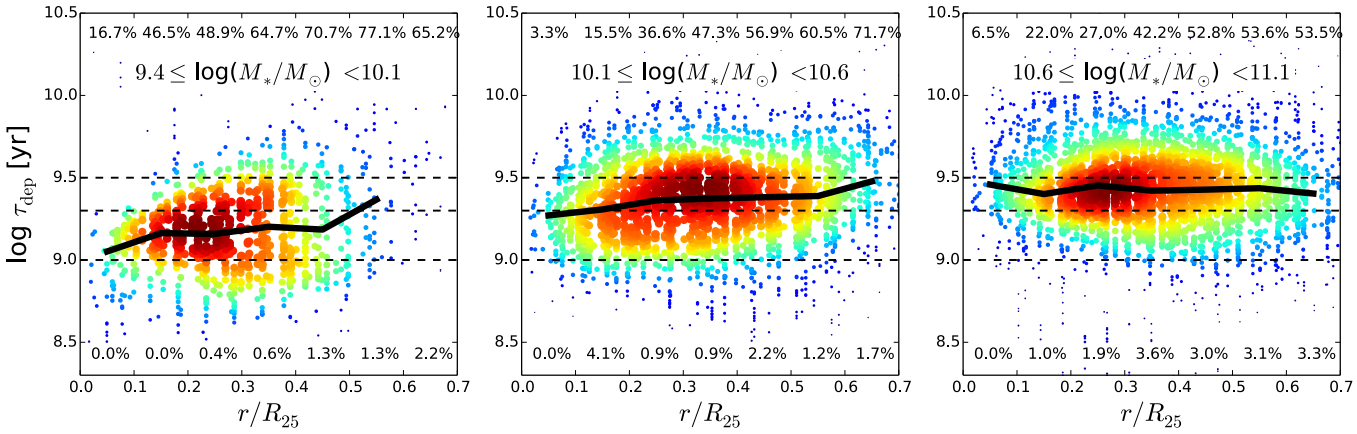

Figure 10. The molecular gas depletion time as a function of radius, separated in three mass bins: $9.6 \leq \log(M_*/M_\odot) < 10.3$ (left panel), $10.3 \leq \log(M_*/M_\odot) < 10.8$ (middle panel), and $10.8 \leq \log(M_*/M_\odot) < 11.3$ (right panel). The colors represent the density of data points. The percentages are the fraction of upper and lower limits at a given radial bin. The solid black lines are the median value of $\tau_{\rm dep}$ at a given radial bin, while the dashed lines are the constant $\tau_{\rm dep}$ values of 1, 2, and 3 Gyrs. This figure shows that the drop of $\tau_{\rm dep}$ in the centers is more prominent in the lowest mass bin.

factor inferred from the increase in metallicity and stellar surface density towards the galactic center would increase the estimated drop in $\tau_{\rm center}$.

2. The drop (rise) of $\tau_{\rm center}$ is caused by higher (lower) central $\Sigma_{\rm SFR}$ than those in the disk, not lower (higher) $\Sigma_{\rm mol}$ (Figure 8). Furthermore, galaxies with higher stellar density contrast in the center (i.e. higher $\Sigma_*^{\rm center}/\Sigma_*^{\rm disk}$) tend to have shorter $\tau_{\rm center}/\tau_{\rm disk}$. Since the dynamical equilibrium pressure depends on Σ_* (Blitz & Rosolowsky 2004, 2006; Ostriker et al. 2010), this suggests that the central drop in $\tau_{\rm dep}$ is driven by high pressure. This is expected for the star formation self-regulated model, in which the star formation rate locally adjusts so that feedback from massive stars offsets turbulent energy dissipation and cooling. A high feedback rate (short $\tau_{\rm dep}$) is required to maintain the high pressure in regions where the vertical gravity from stars and gas is very strong (Ostriker et al. 2010; Ostriker & Shetty 2011; Kim et al. 2011, 2013).

3. The gradient of oxygen abundance is rising toward the center for galaxies in the short $\tau_{\rm center}$ group, while the gradient is flattening in the other groups (Figure 9). This could be the stellar mass effect, where the gradient of oxygen abundance is flattening in massive galaxies (as found by Sánchez-Menguiano et al. 2016), or the oxygen abundance is sensitive to the current star formation efficiency. However, the narrow range of the oxygen abundance variation in our sample (~ 0.2 dex) becomes the limitation of our analysis.

4. There are two signatures for dynamical effects that drive the variation of $\tau_{\rm center}$ versus $\tau_{\rm disk}$. First, the barred and interacting galaxies tend to have lower values of $\log(\tau_{\rm center}/\tau_{\rm disk})$ than the unbarred, isolated galaxies (Figure 6). Second, the size of molecular

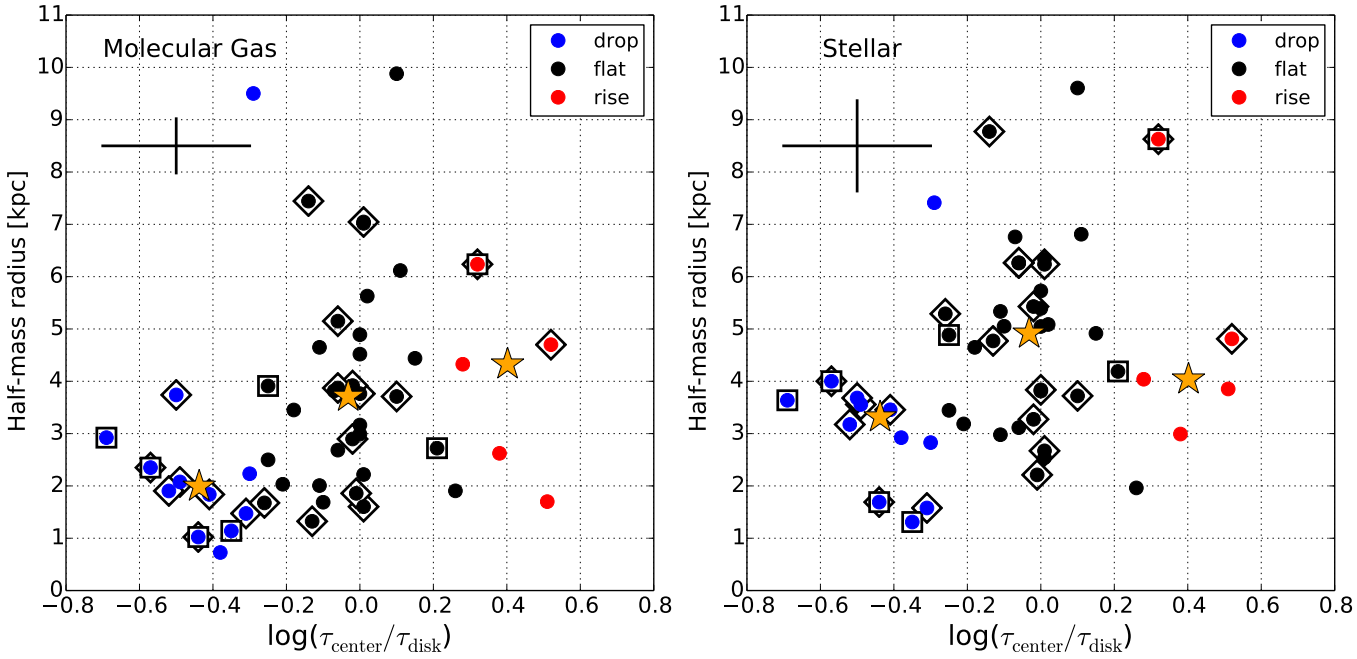

Figure 11. The half-mass radius of molecular gas (left panel) and stars (right panel) for three groups: central drop (blue dots), flat (black dots), and central rise (red dots) of $\tau_{\rm dep}$. The mean values for each three groups are marked as orange stars symbols. The typical errors are shown as crosses. The diamond symbols marked the barred galaxies, while the square symbols marked the interacting galaxies. This shows that the molecular gas distribution in the drop $\tau_{\rm center}$ group and in the disturbed (barred or interacting) galaxies is more compact than those in the other groups.

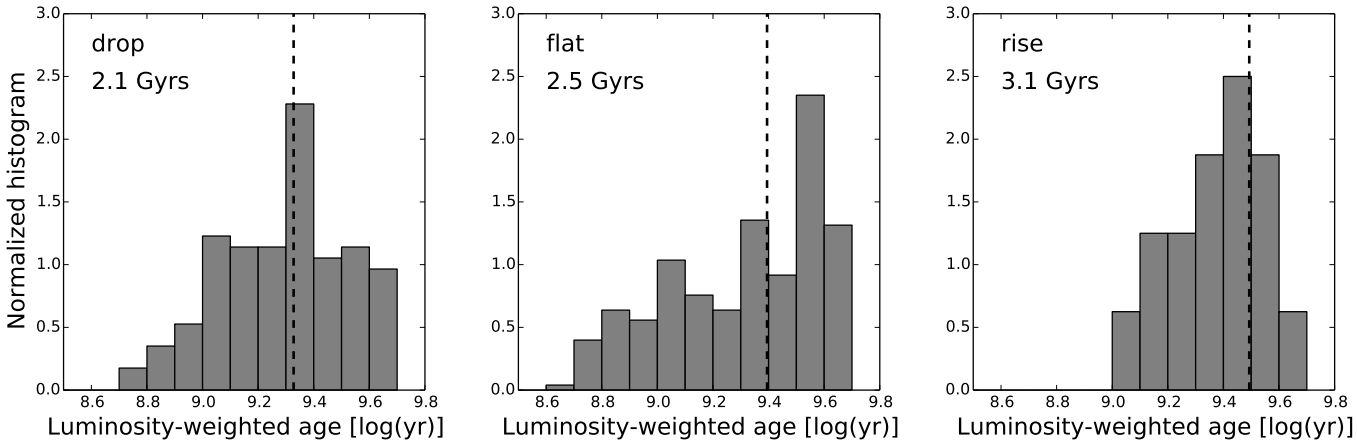

Figure 12. The histogram of luminosity-weighted stellar population ages (from CALIFA; Sánchez et al. 2016) in the center of galaxies ($r \leq 0.1\ R_{25}$) that show a drop of $\tau_{\rm center}$(left panel), flat $\tau_{\rm dep}$ (middle panel), and a rise of $\tau_{\rm center}$ (right panel). The dashed lines mark the median ages, with their values are noted in top left corner of each panels. The stellar populations in the centers of drop $\tau_{\rm center}$ group tend to be younger than the other two groups, consistent with the idea of a bursting period of star formation.

gas disk is smaller in the drop $\tau_{\rm center}$ group than in the other groups (Figure 11). We suspect that the bar drives the gas inward toward the center (or in the case of interacting galaxies, the gas lose its angular momentum). This radial gas compression increases the pressure, resulting in higher star formation efficiency in the galactic center (Krumholz & Kruijssen 2015).

In conclusion, these findings imply that the formation of stars from the molecular gas depends on the local environment within a galaxy (such as Σ_*) and the galaxy dynamics induced by bar or interactions. In the future, we are interested to measure the dense gas (as traced by HCN lines) to investigate whether the short $\tau_{\rm center}$ is also due to a higher fraction of the dense gas in the center. In addition, measuring the shear rate and the inflow speed in barred galaxies will give a better evidence of the importance of galactic dynamics in driving $\tau_{\rm dep}$. Finally, expanding our sample towards early-type and low mass galaxies using ALMA is a natural

approach to expand our statistical sample in the three groups of $\tau_{\rm dep}$.

We thank John Carpenter for his help in managing the schedule of CARMA observations. The works of DU and LB are supported by the National Science Foundation (NSF) under grants AST-1140063 and AST-1616924. ADB and RCL acknowledge support from NSF through grants AST-1412419 and AST-1615960. ADB also acknowledges visiting support by the Alexander von Humboldt Foundation. TW and YC acknowledge support from NSF through grants AST-1139950 and AST-1616199. The work of ECO is supported by the NSF under grant AST-1312006. SFS acknowledges the PAPIIT-DGAPA-IA101217 project and CONACYT-IA-180125. RGB acknowledges support through grant AYA2016-77846-P. ER is supported by a Discovery Grant from NSERC of Canada. SV acknowledges support from NSF AST-1615960. We acknowledge the usage of the HyperLeda database (http://leda.univ-lyon1.fr). Support for the CARMA construction was derived from the states of California, Illinois, and Maryland, the James S. McDonnell Foundation, the Gordon and Betty Moore Foundation, the Kenneth T. and Eileen L. Norris Foundation, the University of Chicago, the Associates of the California Institute of Technology, and NSF. This research is based on observations collected at the Centro Astronomico Hispano Aleman (CAHA) at Calar Alto, operated jointly by the Max-Planck Institute for Astronomy (MPIA) and the Instituto de Astrofisica de Andalucia (CSIC).

APPENDIX

Table 1. The list of galaxy properties in the sample.

No.	Galaxies	RA	Dec	M_*[a]	$M_{\rm mol}$[b]	R_{25}[c]	Beam[d]	Dist.[e]	Inc.[f]	P.A.[f]	$\tau_{\rm center}$	$\tau_{\rm disk}$	$\tau_{\rm med}$	Group	Bar[g]	Inter.[h]
		h:m:s	d:m:s	log($M_\odot$)		kpc	kpc	Mpc	deg.	deg.	log(yr)	log(yr)	log(yr)			
1	IC1151	$15^{\rm h}58^{\rm m}58^{\rm s}.5$	$17^\circ26'26''.5$	9.82	7.93	10.01	0.67	30.80	68.0	208.9	8.94	9.04	8.99	flat	N	N
2	IC1199	$16^{\rm h}10^{\rm m}10^{\rm s}.6$	$10^\circ02'02''.4$	10.58	9.35	11.83	1.52	68.25	64.5	337.3	9.45	9.58	9.56	flat	N	N
3	IC1683	$01^{\rm h}22^{\rm m}22^{\rm s}.6$	$34^\circ26'26''.2$	10.56	9.68	13.34	1.47	69.73	44.8	20.6	9.15	9.64	9.64	drop	Y	N
4	NGC0477	$01^{\rm h}21^{\rm m}21^{\rm s}.3$	$40^\circ29'29''.3$	10.70	9.54	19.29	1.86	85.42	60.0	150.0	9.37	9.68	9.66	drop	N	N
5	NGC0496	$01^{\rm h}23^{\rm m}23^{\rm s}.2$	$33^\circ31'31''.7$	10.64	9.48	11.34	1.82	87.47	57.0	38.5	9.15	9.23	9.22	flat	N	N
6	NGC0551	$01^{\rm h}27^{\rm m}27^{\rm s}.7$	$37^\circ10'11''.0$	10.75	9.39	16.10	1.54	74.50	64.2	320.0	9.62	9.58	9.61	flat	Y	N
7	NGC2253	$06^{\rm h}43^{\rm m}43^{\rm s}.7$	$65^\circ12'12''.4$	10.60	9.62	10.61	1.20	51.16	47.4	300.0	9.37	9.37	9.37	flat	Y	N
8	NGC2347	$07^{\rm h}16^{\rm m}16^{\rm s}.1$	$64^\circ42'42''.6$	10.84	9.56	15.25	1.49	63.75	50.2	189.1	9.48	9.34	9.38	flat	Y	N
9	NGC2730	$09^{\rm h}02^{\rm m}02^{\rm s}.3$	$16^\circ50'50''.3$	9.93	9.00	11.52	1.26	54.78	27.7	260.8	9.13	9.24	9.23	flat	N	N
10	NGC2906	$09^{\rm h}32^{\rm m}32^{\rm s}.1$	$08^\circ26'26''.5$	10.38	9.11	7.44	0.94	37.73	55.7	265.0	9.78	9.34	9.40	rise	N	N
11	NGC3381	$10^{\rm h}48^{\rm m}48^{\rm s}.4$	$34^\circ42'42''.7$	9.68	8.11	6.87	0.50	23.40	30.8	43.1	8.86	9.31	9.30	drop	Y	N
12	NGC3811	$11^{\rm h}41^{\rm m}41^{\rm s}.3$	$47^\circ41'41''.4$	10.44	9.28	13.05	0.96	44.25	42.5	359.0	9.32	9.28	9.31	flat	Y	N
13	NGC3815	$11^{\rm h}41^{\rm m}41^{\rm s}.7$	$24^\circ48'48''.0$	10.32	9.16	11.22	1.14	53.59	59.9	67.8	9.43	9.47	9.45	flat	Y	N
14	NGC3994	$11^{\rm h}57^{\rm m}57^{\rm s}.6$	$32^\circ16'16''.6$	10.39	9.26	5.53	1.02	44.75	59.5	188.1	9.07	8.78	8.81	flat	N	N
15	NGC4047	$12^{\rm h}02^{\rm m}02^{\rm s}.8$	$48^\circ38'38''.2$	10.67	9.66	10.95	1.06	49.06	42.1	105.0	9.41	9.43	9.41	flat	N	N
16	NGC4470	$12^{\rm h}29^{\rm m}29^{\rm s}.6$	$07^\circ49'49''.4$	10.03	8.59	6.23	0.78	33.43	47.5	359.5	8.74	8.87	8.85	flat	N	N
17	NGC4644	$12^{\rm h}42^{\rm m}42^{\rm s}.7$	$55^\circ08'08''.7$	10.48	9.20	15.77	1.60	71.65	72.9	57.0	9.59	9.56	9.57	flat	N	N
18	NGC4711	$12^{\rm h}48^{\rm m}48^{\rm s}.8$	$35^\circ19'20''.0$	10.38	9.18	10.31	1.32	58.83	58.3	215.0	9.60	9.44	9.45	flat	N	N
19	NGC4961	$13^{\rm h}05^{\rm m}05^{\rm s}.8$	$27^\circ44'44''.0$	9.77	8.41	5.93	0.78	36.58	46.6	90.0	9.21	9.23	9.22	flat	Y	N
20	NGC5000	$13^{\rm h}09^{\rm m}09^{\rm s}.8$	$28^\circ54'54''.4$	10.74	9.45	15.04	1.62	80.80	20.0	1.3	9.40	9.59	9.53	flat	Y	N
21	NGC5016	$13^{\rm h}12^{\rm m}12^{\rm s}.1$	$24^\circ05'05''.7$	10.27	8.90	8.45	0.83	36.90	39.9	57.4	9.10	9.43	9.40	drop	N	N
22	NGC5056	$13^{\rm h}16^{\rm m}16^{\rm s}.2$	$30^\circ57'57''.0$	10.64	9.45	19.14	1.96	81.14	61.4	178.0	9.03	8.43	8.51	rise	Y	N
23	NGC5480	$14^{\rm h}06^{\rm m}06^{\rm s}.4$	$50^\circ43'43''.5$	9.97	8.92	6.57	0.52	26.96	41.5	178.0	8.99	9.20	9.20	flat	N	N
24	NGC5520	$14^{\rm h}12^{\rm m}12^{\rm s}.4$	$50^\circ20'20''.9$	9.87	8.67	6.25	0.55	26.73	59.1	245.1	8.99	9.45	9.30	drop	Y	N
25	NGC5633	$14^{\rm h}27^{\rm m}27^{\rm s}.5$	$46^\circ08'08''.8$	10.20	9.14	5.29	0.71	33.38	41.9	16.9	9.25	9.23	9.24	flat	N	N
26	NGC5657	$14^{\rm h}30^{\rm m}30^{\rm s}.7$	$29^\circ10'10''.8$	10.29	9.11	14.34	1.20	56.33	68.3	344.0	9.00	9.55	9.52	drop	Y	N
27	NGC5732	$14^{\rm h}40^{\rm m}40^{\rm s}.7$	$38^\circ38'38''.3$	10.03	8.82	9.66	1.25	54.00	58.4	43.2	9.16	9.42	9.41	flat	N	N
28	NGC5784	$14^{\rm h}54^{\rm m}54^{\rm s}.3$	$42^\circ33'33''.5$	11.09	9.40	17.12	1.67	79.42	45.0	252.0	9.26	10.40	9.95	drop	N	Y
29	NGC5930	$15^{\rm h}26^{\rm m}26^{\rm s}.1$	$41^\circ40'40''.6$	10.40	9.33	10.01	0.83	37.23	45.0	155.0	9.27	10.04	9.71	drop	Y	Y
30	NGC5934	$15^{\rm h}28^{\rm m}28^{\rm s}.2$	$42^\circ55'55''.8$	10.66	9.81	7.35	1.76	82.71	55.0	5.0	10.00	9.77	9.79	flat	N	Y
31	NGC5947	$15^{\rm h}30^{\rm m}30^{\rm s}.6$	$42^\circ43'43''.0$	10.67	9.26	14.61	1.92	86.07	32.2	206.6	9.09	9.61	9.59	drop	Y	N
32	NGC5953	$15^{\rm h}34^{\rm m}34^{\rm s}.5$	$15^\circ11'11''.6$	10.18	9.49	6.09	0.61	28.43	26.1	43.3	9.12	9.60	9.47	drop	N	Y

Table 1 continued

Table 1 *(continued)*

No.	Galaxies	RA	Dec	M_*[a]	$M_{\rm mol}$[b]	R_{25}[c]	Beam[d]	Dist.[e]	Inc.[f]	P.A.[f]	$\tau_{\rm center}$	$\tau_{\rm disk}$	$\tau_{\rm med}$	Group	Bar[g]	Inter.[h]
		h:m:s	d:m:s	log($M_\odot$)		kpc	kpc	Mpc	deg.	deg.	log(yr)	log(yr)	log(yr)			
33	NGC5980	$15^h41^m41^s.5$	$15°47'47''.3$	10.61	9.70	14.10	1.27	59.36	66.2	15.0	9.47	9.15	9.19	rise	N	N
34	NGC6004	$15^h50^m50^s.4$	$18°56'56''.4$	10.66	9.33	15.19	1.22	55.21	37.3	277.3	9.61	9.66	9.63	flat	Y	N
35	NGC6060	$16^h05^m05^s.9$	$21°29'29''.1$	10.78	9.68	17.41	1.28	63.24	64.3	102.0	9.39	9.36	9.38	flat	N	N
36	NGC6155	$16^h26^m26^s.1$	$48°22'22''.0$	10.18	8.94	6.68	0.77	34.60	44.7	130.0	9.02	9.10	9.08	flat	N	N
37	NGC6186	$16^h34^m34^s.4$	$21°32'32''.5$	10.41	9.46	9.68	0.92	42.38	71.2	69.8	9.32	9.49	9.46	flat	Y	N
38	NGC6301	$17^h08^m08^s.5$	$42°20'20''.3$	10.98	9.96	31.24	2.63	121.36	52.8	288.5	9.75	9.61	9.65	flat	N	N
39	NGC7738	$23^h44^m44^s.0$	$00°31'31''.0$	11.01	9.99	16.87	1.90	97.82	65.6	244.7	9.17	10.01	9.74	drop	Y	Y
40	NGC7819	$00^h04^m04^s.4$	$31°28'28''.3$	10.41	9.27	14.99	1.43	71.62	54.0	280.3	9.28	9.55	9.54	flat	Y	N
41	UGC03253	$05^h19^m19^s.7$	$84°03'03''.1$	10.43	8.88	11.88	1.57	59.46	58.3	267.7	8.88	9.31	9.29	drop	Y	N
42	UGC04132	$07^h59^m59^s.2$	$32°54'54''.9$	10.74	10.02	13.51	1.70	75.35	72.0	212.6	9.35	9.41	9.41	flat	Y	N
43	UGC04461	$08^h33^m33^s.4$	$52°31'31''.9$	10.17	9.24	14.51	1.59	72.27	70.1	215.8	9.36	9.35	9.36	flat	N	N
44	UGC05108	$09^h35^m35^s.4$	$29°48'48''.8$	10.90	9.75	18.84	2.81	118.41	66.1	133.1	9.47	9.61	9.53	flat	Y	N
45	UGC07012	$12^h02^m02^s.1$	$29°50'50''.9$	9.70	8.35	6.96	0.92	44.28	60.5	182.1	8.75	9.14	9.13	drop	N	N
46	UGC08107	$12^h59^m59^s.7$	$53°20'20''.5$	11.00	10.11	40.43	2.75	121.62	71.4	233.2	9.92	9.59	9.60	rise	Y	Y
47	UGC09067	$14^h10^m10^s.8$	$15°12'12''.6$	10.76	9.83	13.54	2.75	114.50	62.4	14.6	9.46	9.46	9.46	flat	N	N
48	UGC09476	$14^h41^m41^s.5$	$44°30'30''.8$	10.23	9.15	10.19	1.01	46.63	48.5	312.0	9.32	9.52	9.50	flat	N	N
49	UGC09542	$14^h49^m49^s.0$	$42°27'27''.8$	10.32	9.31	16.64	1.65	79.70	72.7	214.3	9.56	9.56	9.56	flat	N	N
50	UGC09759	$15^h10^m10^s.7$	$55°21'21''.0$	9.81	9.07	9.55	1.03	49.25	66.8	54.7	10.20	9.61	9.69	rise	N	N
51	UGC10205	$16^h06^m06^s.7$	$30°05'05''.9$	10.88	9.60	19.95	2.21	94.92	51.7	118.6	9.56	9.82	9.81	flat	N	Y
52	UGC10710	$17^h06^m06^s.9$	$43°07'07''.3$	10.72	9.88	29.51	2.63	121.69	69.6	329.5	9.61	9.50	9.50	flat	N	N

[a] The stellar mass assuming Kroupa IMF from the CALIFA survey (Sánchez et al. 2016).

[b] The molecular gas mass assuming CO-to-H_2 conversion factor of 4.4 $M_\odot$ pc^{-2} (K km s^{-1} pc^2)$^{-1}$ from the EDGE survey (Bolatto et al. 2017), including mass contribution from Helium.

[c] The radius where the surface brightness is 25 mag/arcsec^2 in the $B-$band, from the HyperLEDA catalog (Makarov et al. 2014).

[d] The physical beam size, calculated from the geometric mean of the EDGE beam size.

[e] The luminosity distance computed from the CALIFA redshift for ionized gas lines assuming $H_0 = 70$ km s^{-1}, $\Omega_{\rm m} = 0.27$, and $\Omega_\Lambda = 0.73$.

[f] The inclination and position angle are taken from the following, ordered by priority: (1) the best fit of CO rotation curve (Levy et al. in preparation), whenever it is possible, (2) from the shape of the outer isophote, or (3) from the HyperLEDA catalog (Makarov et al. 2014).

[g] The bar assignments (`Yes` or `No`) are taken from the following, ordered by priority: (1) the photometric fit from Méndez-Abreu et al. (2017), or (2) the HyperLEDA catalog (Makarov et al. 2014).

[h] The assignment for interacting galaxies (`Yes` or `No`), taken from Barrera-Ballesteros et al. (2015).

REFERENCES

Abazajian, K. N., Adelman-McCarthy, J. K., Agüeros, M. A., et al. 2009, ApJS, 182, 543

Allende Prieto, C., Lambert, D. L., & Asplund, M. 2001, ApJL, 556, L63

Alloin, D., Collin-Souffrin, S., Joly, M., & Vigroux, L. 1979, A&A, 78, 200

Baldwin, J. A., Phillips, M. M., & Terlevich, R. 1981, PASP, 93, 5

Barrera-Ballesteros, J. K., García-Lorenzo, B., Falcón-Barroso, J., et al. 2015, A&A, 582, A21

Bauermeister, A., Blitz, L., & Ma, C.-P. 2010, ApJ, 717, 323

Belfiore, F., Maiolino, R., Maraston, C., et al. 2016, MNRAS, 461, 3111

Bigiel, F., Leroy, A., Walter, F., et al. 2008, AJ, 136, 2846

Bigiel, F., Leroy, A. K., Walter, F., et al. 2011, ApJL, 730, L13

Blitz, L., & Rosolowsky, E. 2004, ApJL, 612, L29

—. 2006, ApJ, 650, 933

Bock, D. C.-J., Bolatto, A. D., Hawkins, D. W., et al. 2006, in Proc. SPIE, Vol. 6267, Society of Photo-Optical Instrumentation Engineers (SPIE) Conference Series, 626713

Bolatto, A. D., Leroy, A. K., Rosolowsky, E., Walter, F., & Blitz, L. 2008, ApJ, 686, 948

Bolatto, A. D., Wolfire, M., & Leroy, A. K. 2013, ARA&A, 51, 207

Bolatto, A. D., Leroy, A. K., Jameson, K., et al. 2011, ApJ, 741, 12

Calzetti, D., Armus, L., Bohlin, R. C., et al. 2000, ApJ, 533, 682

Calzetti, D., Kennicutt, R. C., Engelbracht, C. W., et al. 2007, ApJ, 666, 870

Cardelli, J. A., Clayton, G. C., & Mathis, J. S. 1989, ApJ, 345, 245

Catalán-Torrecilla, C., Gil de Paz, A., Castillo-Morales, A., et al. 2015, A&A, 584, A87

Colombo, D., Hughes, A., Schinnerer, E., et al. 2014, ApJ, 784, 3

Daddi, E., Elbaz, D., Walter, F., et al. 2010, ApJL, 714, L118

de Vaucouleurs, G., de Vaucouleurs, A., Corwin, Jr., H. G., et al. 1991, Third Reference Catalogue of Bright Galaxies. Volume I: Explanations and references. Volume II: Data for galaxies between 0^h and 12^h. Volume III: Data for galaxies between 12^h and 24^h.

Domínguez, A., Siana, B., Henry, A. L., et al. 2013, ApJ, 763, 145

Elmegreen, B. G. 1997, in Revista Mexicana de Astronomia y Astrofisica Conference Series, Vol. 6, Revista Mexicana de Astronomia y Astrofisica Conference Series, ed. J. Franco, R. Terlevich, & A. Serrano, 165
Falcón-Barroso, J., Sánchez-Blázquez, P., Vazdekis, A., et al. 2011, A&A, 532, A95
García-Benito, R., Zibetti, S., Sánchez, S. F., et al. 2015, A&A, 576, A135
Genzel, R., Tacconi, L. J., Gracia-Carpio, J., et al. 2010, MNRAS, 407, 2091
Genzel, R., Tacconi, L. J., Lutz, D., et al. 2015, ApJ, 800, 20
Glover, S. C. O., & Clark, P. C. 2012, MNRAS, 426, 377
Helfer, T. T., Thornley, M. D., Regan, M. W., et al. 2003, ApJS, 145, 259
Hughes, A., Wong, T., Ott, J., et al. 2010, MNRAS, 406, 2065
Hughes, A., Meidt, S. E., Colombo, D., et al. 2013, ApJ, 779, 46
Jameson, K. E., Bolatto, A. D., Leroy, A. K., et al. 2016, ApJ, 825, 12
Jogee, S., Scoville, N., & Kenney, J. D. P. 2005, ApJ, 630, 837
Kauffmann, G., Heckman, T. M., Tremonti, C., et al. 2003, MNRAS, 346, 1055
Kennicutt, R. C., & Evans, N. J. 2012, ARA&A, 50, 531
Kennicutt, Jr., R. C. 1998a, ARA&A, 36, 189
—. 1998b, ApJ, 498, 541
Kewley, L. J., & Dopita, M. A. 2002, ApJS, 142, 35
Kim, C.-G., Kim, W.-T., & Ostriker, E. C. 2011, ApJ, 743, 25
Kim, C.-G., Ostriker, E. C., & Kim, W.-T. 2013, ApJ, 776, 1
Kroupa, P. 2001, MNRAS, 322, 231
Kruijssen, J. M. D., & Longmore, S. N. 2014, MNRAS, 439, 3239
Krumholz, M. R., Dekel, A., & McKee, C. F. 2012, ApJ, 745, 69
Krumholz, M. R., & Kruijssen, J. M. D. 2015, MNRAS, 453, 739
Krumholz, M. R., Leroy, A. K., & McKee, C. F. 2011, ApJ, 731, 25
Leroy, A., Bolatto, A., Stanimirovic, S., et al. 2007, ApJ, 658, 1027
Leroy, A. K., Walter, F., Brinks, E., et al. 2008, AJ, 136, 2782
Leroy, A. K., Walter, F., Bigiel, F., et al. 2009, AJ, 137, 4670
Leroy, A. K., Bolatto, A., Gordon, K., et al. 2011, ApJ, 737, 12
Leroy, A. K., Bigiel, F., de Blok, W. J. G., et al. 2012, AJ, 144, 3
Leroy, A. K., Walter, F., Sandstrom, K., et al. 2013, AJ, 146, 19
Lilly, S. J., Carollo, C. M., Pipino, A., Renzini, A., & Peng, Y. 2013, ApJ, 772, 119
Madau, P., & Dickinson, M. 2014, ARA&A, 52, 415
Makarov, D., Prugniel, P., Terekhova, N., Courtois, H., & Vauglin, I. 2014, A&A, 570, A13
Marino, R. A., Rosales-Ortega, F. F., Sánchez, S. F., et al. 2013, A&A, 559, A114
Martins, L. P., González Delgado, R. M., Leitherer, C., Cerviño, M., & Hauschildt, P. 2005, MNRAS, 358, 49
McKee, C. F., & Ostriker, E. C. 2007, ARA&A, 45, 565
Méndez-Abreu, J., Ruiz-Lara, T., Sánchez-Menguiano, L., et al. 2017, A&A, 598, A32
Oka, T., Hasegawa, T., Sato, F., et al. 2001, ApJ, 562, 348
Osterbrock, D. E. 1989, Astrophysics of gaseous nebulae and active galactic nuclei
Ostriker, E. C., McKee, C. F., & Leroy, A. K. 2010, ApJ, 721, 975
Ostriker, E. C., & Shetty, R. 2011, ApJ, 731, 41
Pettini, M., & Pagel, B. E. J. 2004, MNRAS, 348, L59
Rahman, N., Bolatto, A. D., Xue, R., et al. 2012, ApJ, 745, 183
Rosolowsky, E., & Blitz, L. 2005, ApJ, 623, 826
Rosolowsky, E., & Leroy, A. 2006, PASP, 118, 590
Saintonge, A., Kauffmann, G., Kramer, C., et al. 2011a, MNRAS, 415, 32
Saintonge, A., Kauffmann, G., Wang, J., et al. 2011b, MNRAS, 415, 61
Salpeter, E. E. 1955, ApJ, 121, 161
Sánchez, S. F., Kennicutt, R. C., Gil de Paz, A., et al. 2012, A&A, 538, A8
Sánchez, S. F., Rosales-Ortega, F. F., Iglesias-Páramo, J., et al. 2014, A&A, 563, A49
Sánchez, S. F., Pérez, E., Sánchez-Blázquez, P., et al. 2016, RMxAA, 52, 171
Sánchez-Blázquez, P., Peletier, R. F., Jiménez-Vicente, J., et al. 2006, MNRAS, 371, 703
Sánchez-Menguiano, L., Sánchez, S. F., Pérez, I., et al. 2016, A&A, 587, A70
Sandstrom, K. M., Leroy, A. K., Walter, F., et al. 2013, ApJ, 777, 5
Sault, R. J., Teuben, P. J., & Wright, M. C. H. 1995, in Astronomical Society of the Pacific Conference Series, Vol. 77, Astronomical Data Analysis Software and Systems IV, ed. R. A. Shaw, H. E. Payne, & J. J. E. Hayes, 433
Schinnerer, E., Meidt, S. E., Pety, J., et al. 2013, ApJ, 779, 42
Schmidt, M. 1959, ApJ, 129, 243
Schruba, A., Leroy, A. K., Walter, F., Sandstrom, K., & Rosolowsky, E. 2010, ApJ, 722, 1699
Schruba, A., Leroy, A. K., Walter, F., et al. 2011, AJ, 142, 37
—. 2012, AJ, 143, 138
Silk, J. 1997, ApJ, 481, 703
Singh, R., van de Ven, G., Jahnke, K., et al. 2013, A&A, 558, A43
Spergel, D. N., & Blitz, L. 1992, Nature, 357, 665
Vazdekis, A., Sánchez-Blázquez, P., Falcón-Barroso, J., et al. 2010, MNRAS, 404, 1639
Walcher, C. J., Wisotzki, L., Bekeraité, S., et al. 2014, A&A, 569, A1
Weisz, D. R., Johnson, B. D., Johnson, L. C., et al. 2012, ApJ, 744, 44
Wong, T., & Blitz, L. 2002, ApJ, 569, 157
Wong, T., Xue, R., Bolatto, A. D., et al. 2013, ApJL, 777, L4
Wright, E. L., Eisenhardt, P. R. M., Mainzer, A. K., et al. 2010, AJ, 140, 1868